Atomically Thin Half-van der Waals Metals Enabled by Confinement Heteroepitaxy

Natalie Briggs[1,2,3†], Brian Bersch[1,2†], Yuanxi Wang[2,3], Jue Jiang[4], Roland J. Koch[5,6], Nadire Nayir[3,7], Ke Wang[8], Marek Kolmer[9], Wonhee Ko[9], Ana De La Fuente Duran[1], Shruti Subramanian[1,2], Chengye Dong[1,2], Jeffrey Shallenberger[8], Mingming Fu[9], Qiang Zou[9], Ya-Wen Chuang[4], Zheng Gai[9], An-Ping Li[9], Aaron Bostwick[5], Chris Jozwiak[5], Cui-Zu Chang[4], Eli Rotenberg[5], Jun Zhu[4], Adri C. T. van Duin[1,3,7,8,10,11,12], Vincent Crespi[2,3,8,4], Joshua A. Robinson[1,2,3,8,13*]

[1]Department of Materials Science and Engineering, The Pennsylvania State University, University Park, PA 16802, United States of America
[2]Center for 2-Dimensional and Layered Materials, The Pennsylvania State University, University Park, PA 16802, United States of America
[3]2-Dimensional Crystal Consortium, The Pennsylvania State University, University Park, PA 16802, United States of America
[4]Department of Physics, The Pennsylvania State University, University Park, PA 16802, United States of America
[5]Advanced Light Source, Lawrence Berkeley National Laboratory, Berkeley, California 94720, United States of America
[6]The Molecular Foundry, Lawrence Berkeley National Laboratory, Berkeley, California 94720, United States of America
[7]Department of Mechanical Engineering, The Pennsylvania State University, University Park, PA 16802, United States of America
[8]Materials Research Institute, The Pennsylvania State University, University Park, PA 16802, United States of America
[9]Center for Nanophase Materials Sciences, Oak Ridge National Laboratory, Oak Ridge, TN 37831, United States of America
[10]Department of Chemistry, The Pennsylvania State University, University Park, PA 16802, United States of America
[11]Department of Engineering Science & Mechanics, The Pennsylvania State University, University Park, PA 16802, United States of America
[12]Department of Chemical Engineering, The Pennsylvania State University, University Park, PA 16802, United States of America
[13]Center for Atomically Thin Multifunctional Coatings, The Pennsylvania State University, University Park, PA 16802, United States of America
†Equally contributing authors
*Corresponding author
Email: jrobinson@psu.edu

Atomically thin two-dimensional (2D) metals may be key ingredients in next-generation quantum and optoelectronic devices. However, 2D metals must be stabilized against environmental degradation and integrated into heterostructure devices at the wafer scale. The high-energy interface between silicon carbide and epitaxial graphene provides an intriguing framework for stabilizing a diverse range of 2D metals. Here we demonstrate large-area, environmentally stable, single-crystal 2D gallium, indium, and tin. These 2D metals are covalently bonded to SiC below but present a non-bonded interface to graphene overlayer, i.e. they are "half van der Waals" metals with strong internal gradients in

bonding character. These non-centrosymmetric 2D metals open compelling opportunities for superconducting devices, topological phenomena, and advanced optoelectronic properties. For example, air-stable 2D-Ga is a superconductor that combines six strongly coupled Ga-derived electron pockets with a large nearly-free-electron Fermi surface that closely approaches the Dirac points of the graphene overlayer.

Major advances in fundamental science have followed from the exfoliation, stacking, and encapsulation of atomically thin 2D layers[1]. The next step towards technological impact of 2D layers and heterostructures is to transition sophisticated "pick and place" devices to a *wafer-scale* platform. However, the sensitivity of 2D systems to interfacial reactions and environmental influences – especially for two-dimensional metals or small-gap semiconductors – poses challenges for large-scale integration. Very few metals resist degradation of their top few atomic layers upon environmental exposure, and for a 2D metal, these layers constitute the entire system. A general platform for producing *environmentally stable* and *wafer-scale* 2D metals that are not prone to interfacial interactions would represent a significant advance. Inspired by the success of wide-bandgap 2D gallium nitride,[2] we turn focus onto the metal alone and demonstrate a platform dubbed **confinement heteroepitaxy** (CHet), where the interface between epitaxial graphene and silicon carbide[3] stabilizes crystalline 2D forms of Group-III (Ga, In) and group-IV (Sn) elements. Defect engineering of the graphene overlayer enables uniform, large-area intercalation as a surfactant at the high-energy SiC/EG interface; this interface then templates intercalant crystallization at a thermodynamically defined number of atomic layers. The unreactive nature of as-grown epitaxial graphene on SiC (graphene plus buffer layer) performs multiple services: (1) it only partially passivates the SiC surface underneath, thereby sustaining the high-energy interface that drives intercalation; (2) it lowers the energy of the (otherwise exposed) upper surface of the metal, thus facilitating 2D morphologies; (3) it protects the newly formed 2D metal from environmental degradation after intercalation through *in situ* healing of the graphene defects. Stability of these 2D metals in air over months greatly facilitates *ex situ* characterization and enables facile processing and device fabrication. Competing methods to obtain thin crystalline metal films are specific to certain metallic species (e.g. Au[4] or TiN[5]) and generally produce thicker, few-nm layers without *in situ* encapsulation, whereas CHet produces stable atomically-thin crystalline 2D forms of diverse metals which do not otherwise exist in nature.

Discussion

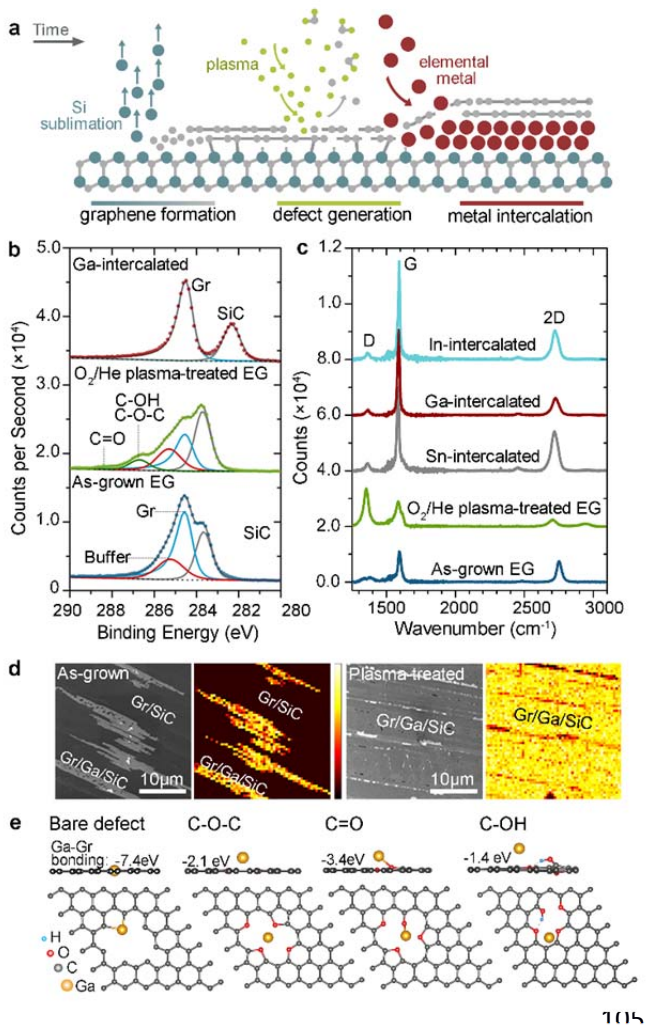

Figure 1: **Confinement Heteroepitaxy in defect-engineered epitaxial graphene.** (a) Schematic of CHet showing EG growth, O_2/He plasma treatment and intercalation steps. (b) XPS showing C 1s for (bottom) as-grown EG, (middle) O_2/He plasma-treated EG, and (top) Ga-intercalated EG demonstrating the creation and annihilation of C-O bonds during CHet; this is confirmed by (c) Raman spectroscopy of as-grown EG, O_2/He plasma-treated EG, and metal-intercalated EG, where the defect peak (D peak) is dramatically reduced as a result of the intercalation process. The SiC background Raman spectra are subtracted from the acquired EG/SiC Raman. (d) SEM and accompanying AES maps demonstrate that defects formed due to plasma treatments lead to significantly improved intercalation uniformity, with >95% surface coverage when the EG is plasma treated. (e) DFT modelling of Ga atoms on optimized graphene sheets with bare, C−O−C, C=O, and C−OH passivated defects suggests that oxygen termination (e) provides favorable energies for metal attraction and intercalation through the graphene sheet. The Ga binding energy to each defect is shown in each model.

Unlike traditional EG intercalation methods[6–9], CHet (**Figure 1a**) uses plasma-treated EG and high-pressure (300 Torr) thermal evaporation to realize continuous films of crystalline 2D metals. Nominally monolayer epitaxial graphene is grown by silicon sublimation from 6H-SiC(0001),[10] after which exposure to an oxygen plasma generates defects in the EG layers. Metallic precursors such as Ga, Sn, and In situated in a crucible directly beneath EG are then heated with the EG/SiC to 700–800°C. The vaporized metal diffuses through EG defects to reach the EG/SiC interface. X-ray photoelectron spectroscopy (XPS) (**Figure 1b**) and Raman spectroscopy (**Figure 1c**) reveal how the graphene defects evolve during CHet. O_2/He plasma treatments create defects in the graphene layers that contain C=O and C–OH and/or C–O–C bonds visible in the carbon 1s spectra (**Figure 1b**)[11,12]; these correlate with a 15× increase in the Raman D:G intensity ratio (I_D/I_G) (**Figure 1c**)[13]. Upon metal intercalation, signatures of carbon-oxygen bonding and the EG buffer layer peak disappear from the carbon 1s region (**Figure 1b**), and a metallic Ga 3d peak appears (**Figure S1**). Ultimately, metal intercalation (Ga, In, or Sn) releases the buffer layer[6–8] and removes carbon-oxygen bonding. XPS signatures remain stable even after >8 months in air (**Figure S2**). Intercalation also yields a pronounced (~5×) decrease in I_D relative to plasma-treated EG, and a 3–4× and 1–2× increase in I_G and I_{2D}, respectively, relative to as-grown EG (**Figure 1c**). The decreased I_D, lack of D′ and D+G modes, loss of carbon-oxygen bonding, and air stability of resulting 2D metals all suggest that the graphene heals during intercalation at elevated temperatures[14–16] and subsequently acts as a barrier to oxidation post-synthesis. The strengthening of I_G and I_{2D} after intercalation may be attributed to metal/graphene charge transfer and/or plasmon resonance[17–19]. Comparison of Auger electron

spectroscopy (AES) (**Figures 1d, S3)** and Raman mapping (**Figure S4**) of EG/Ga samples prepared using pristine vs. plasma-treated EG reveals that plasma-treatments greatly increase the lateral coverage of intercalated Ga. Beyond a simple increase in intercalation sites, first-principles calculations suggest that Ga/EG bonding is strengthened with increasing vacancy size, where large, *un-passivated* defects bond covalently with Ga (**Figures 1e**, **S5**). First-principles calculations suggest that the termination of multivacancy graphene defects with oxygen moieties facilitates metal adhesion and transport to the underlying EG/SiC interface through intermediate metal binding energies that are weaker than those of unpassivated vacancies but stronger than those for hydroxyl terminations or the basal plane (**Figures 1e, S5**).

Two dimensional Ga, In, and Sn are 1–3 atomic layers thick and highly registered to the SiC substrate (**Figure 2a,c,e**). The dominant thickness observed can be explained by first-principles equilibrium phase stability calculations (**Figures 2b, d, f, S6**) that predict the layer thickness as a function of metal chemical potential. Strong metal-SiC bonding stabilizes a thin 2D metal compared to the bulk 3D form, but this advantage is diluted by successive thickening of the intercalant so that the bulk phase is preferred beyond a certain thickness. These calculations predict a stability range of 1–3 layers for Ga, 1–2 layers for In, and 1 layer for Sn, all in encouragingly close agreement with scanning transmission electron microscopy (STEM) images (**Figure 2a, c, e**), which display 2–3 layers for Ga, 2 for In, and 1–2 for Sn (in the case of Sn, the blurring of the second Sn layer indicates a lower structural stability for this layer). This close correspondence suggests near-equilibrium growth conditions during CHet, i.e. a relatively high metal atom mobility, which is supported by the uniform metal coverage achieved. The high energy of the initial EG/SiC interface, which follows from the ineffectiveness of graphene in terminating SiC dangling bonds, provides a strong thermodynamic driving force to 2D metal formation, suggesting a broader applicability of CHet to support additional species as 2D metals. The metal thicknesses shown in **Figure 2a ,c, e** are uniform across the terraces of SiC, although

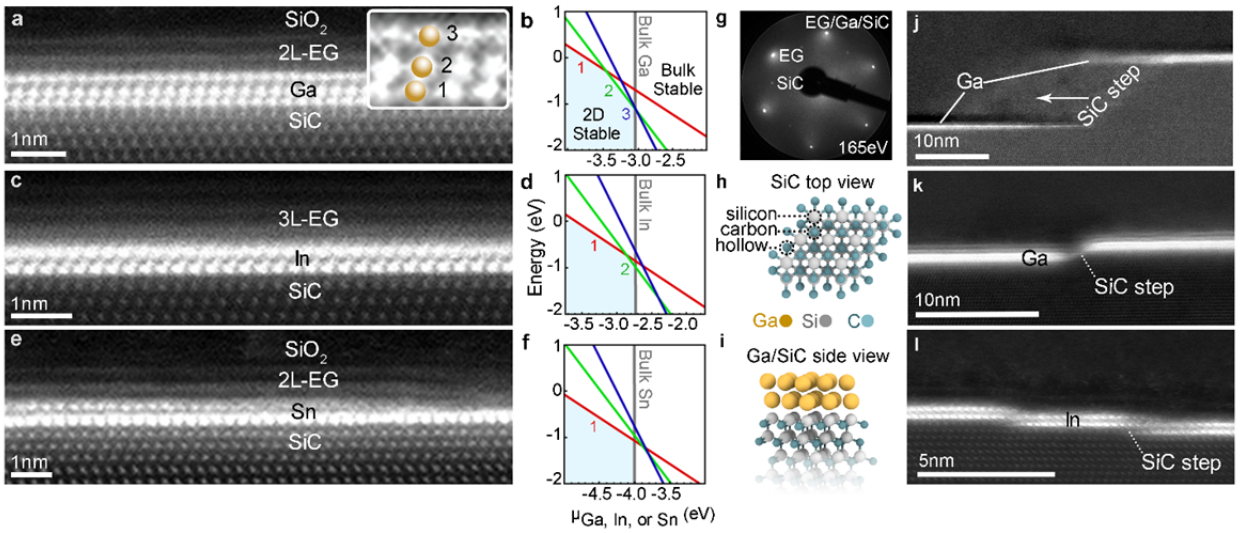

Figure 2: Atomic Structure of CHet-grown 2D metals. (a) Cross-sectional STEM showing 3 layers of Ga between EG and SiC, and (b) corresponding energy minimization calculations showing preferred intercalant layer numbers, with (c-f) showing cross-sectional STEM and layer number calculations for In and Sn. Energy dispersive x-ray spectroscopy (**Figure S7**) confirms that intercalant layers match the respective precursor elements and are not oxidized. The grey, vertical lines in b, d, and f indicate the metal chemical potential of the bulk metal, and red, green, and blue lines indicate energy as a function of chemical potential for 1, 2, and 3 layers, respectively. The lowest line at a given potential indicates the ground state layer-number. (g) Acquired LEED pattern for EG/Ga/SiC indicating the presence of EG and SiC with no additional spots for a unique Ga (or In, Sn – **Figure S8**) structure, indicating the Ga is lattice matched to EG or SiC. (h) Top-down schematic of hexagonal SiC with different sites labeled, where (i) the intercalated Ga layers exhibit an "ABC" stacking over the SiC substrate. (j-l) Step bunching in the SiC surface can lead to discontinuities in the 2D metals, necessitating that SiC steps be single–few atoms in height to maintain structural and electrical continuity.

some SiC terraces show uniform 2L Ga.

An epitaxial relationship of the 2D metals to the SiC substrate is further supported by the observation in low-energy electron diffraction (LEED) of graphene and SiC patterns, but no distinct spots corresponding to a structurally unique intercalant layer (**Figures 2g, S8**); i.e. the SiC diffraction pattern is shared by the metal. The 2.72 Å lateral Ga spacing observed via STEM also closely matches that of SiC (**Figure 2a, S9**). First-principles structural optimization provides further insights into the epitaxial relationship of Ga to SiC (0001). Structural relaxations were performed for 1–3 layers of Ga initialized at sites projecting onto the silicon, carbon, and/or hollow sites of SiC (**Figures 2h, S10, S11, Table S1**). Adding a top bilayer graphene only affects band fillings without changing the relative stability of the Ga structures, so it is not considered in these structural stability calculations. The ground-state locations for the first, second, and third layers of Ga are above the silicon (Ga_{Si}), carbon (Ga_C), and hollow (Ga_{hollow}) sites respectively (**Figure 2i**). This "ABC" stacking resembles a face-centered-cubic lattice cleaved along (111), matching the hexagonal arrangement of SiC (0001) and is possibly related to the metastable distorted FCC phase of Ga-III[20]. Ga registry weakens for increased metal thickness: the Ga_{Si} stacking site for single-layer Ga is 0.14 eV more stable than Ga_C and Ga_{hollow}, but the ground states of Ga multilayers are preferred by only 0.05 eV against competing phases. Cross-sectional STEM (**Figure 2a**, inset) supports the calculated evolution with increasing thickness, where the interlayer spacing between the first and second Ga layers (2.19 Å) is significantly smaller than the second and third (2.36 Å). Density functional theory results show a pronounced shift from largely covalent bonding in the bottom Ga layer (templated against SiC) to comparably strong but more metallic bonding between the upper Ga layers and much weaker interaction between the upper Ga layer and the graphene overlayer (Table S1). Experimentally, epitaxy and metal continuity are interrupted by large steps in the SiC surface (**Figure 2j**), while smaller steps (**Figure 2k**) are less disruptive and single-atom steps (**Figure 2l**) are metal-continuous and appear to maintain epitaxy across the step.

The structural quality of 2D-Ga is reflected in the excellent agreement of ARPES measurements with calculations of the structurally optimized epitaxial system (**Figure 3a,** also **Figure S12** for 2D In). The high valence electron count of *p* block metals and the small lateral unit cell of epitaxial 2D-Ga yield an exceptionally large *s*-band Fermi velocity of 2×10^6 m/s, comparable to that of bulk Al and Ga (assuming a free electron model)[21] or indium on Si(111)[22] and substantially larger than the band velocity of graphitic π states[23,24]. The calculated band structure (**Figure 3b**) shows color-coded projections of the total wavefunction onto the plane-wave components of the graphene (black) and Ga/SiC (blue) primitive cell, where bands are unfolded from the supercell Brillouin zone[25]. The most prominent features are three avoided crossings between *s* and *p* Ga bands, one along Γ-M_{Ga} and two along Γ-K_{Ga} (comparing to a freestanding frozen bilayer of Ga, **Figure S13**, the Ga *s*-band starts ~9 eV below the Fermi level). A large Ga-derived near-free-electron-like Fermi surface (**Figure 3c, d**) closely approaches the graphene Dirac points at K_{gr} and K'_{gr} with further electron pockets around the corners of the Ga Brillouin zone. The position of the graphene Dirac point 0.2–0.3 eV below the Fermi level (**Figure S14**) indicates that Ga (or indium, **Figure S12**) electron dopes graphene by $8–10\times10^{12}$ cm^{-2}. This is supported by the Fermi surface of bilayer Ga/SiC calculated without graphene (**Figure 3e**) where the Fermi level is upshifted by 0.4 eV to be consistent with the measured ARPES band alignment (see **Figure S11**); this artificial upshift is not needed when using hybrid functionals, which

generally yield more accurate band alignments (see SI for details on supercell strain imposed in calculations). Finally, the measured Fermi surface clearly shows that the graphene Brillouin zone

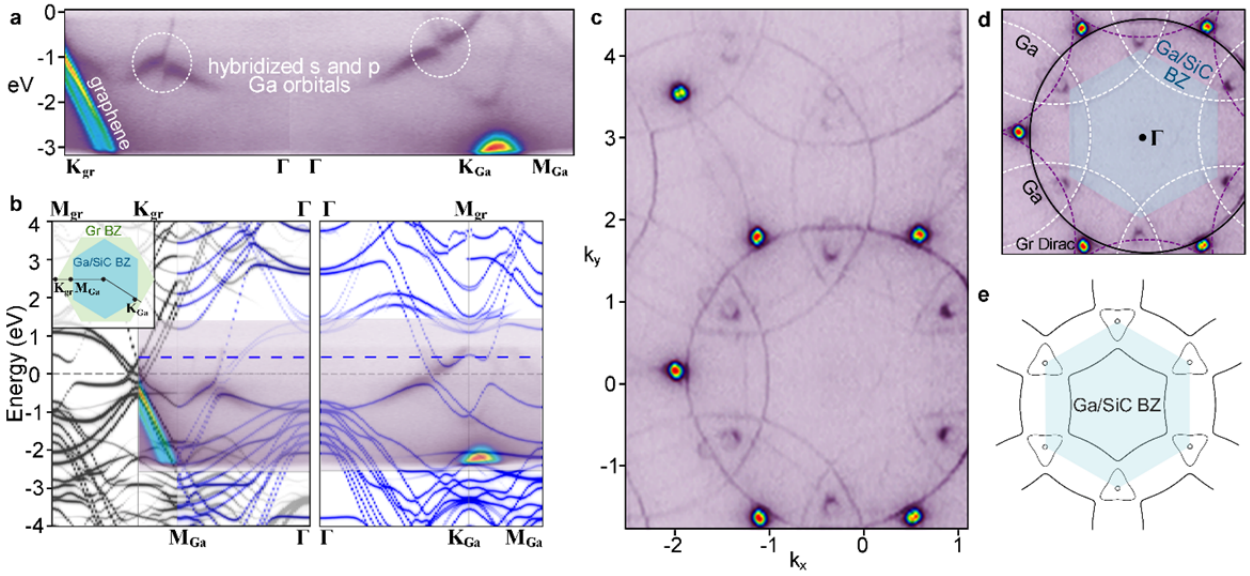

Figure 3: Electronic Structure of CHet-grown 2D Ga. (a) Measured ARPES spectra for EG/Ga/SiC showing graphene and Ga bands near M_{Ga} and K_{Ga} and (b) Calculated band structure in black and blue overlaid with measured ARPES (purple). The effective unfolded band structures of 2×2 graphene + √3×√3 R30º bilayer Ga/SiC along the ΓM_{Ga} (ΓK_g) and the ΓK_{Ga} (ΓM_g) directions are projected onto graphene (black) and Ga/SiC (blue), as indicated by the Brillouin zone paths in the inset (M_{gr} in the left panel and M_{Ga} on the right are from repeated zones). ARPES measurements along the same paths are superimposed. (c, d) ARPES-measured Fermi surface showing nearly-free-electron-like circular contours. Superimposed black, white, and purple circles in (d) correspond to nearly free electron like circular contours from Ga and are drawn to aid in comparison of experimental data with (e) DFT-calculated Fermi surface of bilayer Ga/SiC with the Fermi level shifted (to the blue dashed line in panel (b)) to match the measured band filling.

is rotated 30° from the underlying Ga/SiC zone; providing direct evidence for orientational epitaxy between Ga and SiC.

The air stability of 2D metals formed by CHet enables *ex situ* transport measurements without complex capping methodologies. A co-linear four-point-probe indium dot configuration reveals a largely metallic behavior for 2D-Ga on small-step SiC from room temperature down to 4 K, below which a sharp 4-order-of-magnitude drop in resistance occurs (**Figure 4a**). Following definitions in Methods, T_c^{onset} = 3.95 K, and T_c^{zero} = 3.2 K, i.e. higher than in bulk orthorhombic α-Ga (1.08K)[26], similar to that of metastable monoclinic β-Ga (5.9–6.5K), and below that of metastable amorphous Ga (8.4 K)[27–29]. As expected, the transition drops and broadens with increasing perpendicular magnetic field $B_\perp$ (**Figure 4b**). R versus $B_\perp$ indicates B_c = 130 mT at 2 K with a corresponding coherence length ξ_0 ~ 50 nm (**Figure 4c**, **Methods**). A linear extrapolation of $B_c(T)$ from R(B) suggests a zero-Kelvin critical field $B_{c0} \approx$ 260 mT and ξ_0 ~ 36 nm, higher than that of α-Ga ($B_{c0} \approx$ 6 mT)[26] and β-Ga ($B_{c0} \approx$ 54 mT)[29] (**Figure S15a**). Considering the very high Fermi velocity and moderate T_c, the system is likely not in the clean limit. Scanning tunneling microscopy/spectroscopy show quite uniform differential tunneling conductance (dI/dV) spectra at multiple locations on the sample (**Figure 4d,f, S15**). A superconducting gap with well-defined coherence peaks at ±0.6 meV is seen at 2.2 K (**Figure 4h**) and disappears at ~3 K, below the transport T_c (**Figure 4g**), perhaps due to a moderately reduced proximity-induced superconducting order parameter in the 2–3L graphene overlayer[30].

The observation of a significant superconducting order parameter at the upper graphene surface bodes well for the formation of superconducting heterostructures via proximity effect.

When crystallographic steps on SiC(0001) are less than 1 nm tall (**Figure 2k,l**), transport measurements that orient the current parallel or perpendicular to the steps have similar $T_c^{onset} \sim 4$ K and $T_c^{zero} \sim 3.2$ K (**Figure 4i**). Although steps more than 5 nm tall (**Figure 2j, 4j**) yield similar $T_c^{onset} \sim 3.8$ K for both directions, only parallel transport displays a fully developed superconducting transition with $T_c^{zero} \sim 2.5$ K, suggesting that transport perpendicular to large steps encounters a finite series resistance at the steps. Small-step 2D-Ga exhibits a Berezinskii-Kosterlitz-Thouless transition temperature[31] of $T_{BKT}=3.1$K (2.9K) for transport parallel (perpendicular) to the SiC steps (**Figure S17**), indicating a largely isotropic 2D superconducting transition in these samples. Note that I-V measurements up to the critical current (I_c) are limited by the experimental setup, and T_{BKT} is likely closer to 3.88 K (**Figure S17**) if extracted from curves closer to I_c. Full R(T) and R(B) curves for "large-step" 2D-Ga are provided in **Figure S18**. Epitaxial graphene synthesis must limit step bunching to ensure uniform superconducting films with isotropic transport. SiC step height and bunching can be mitigated by reducing the

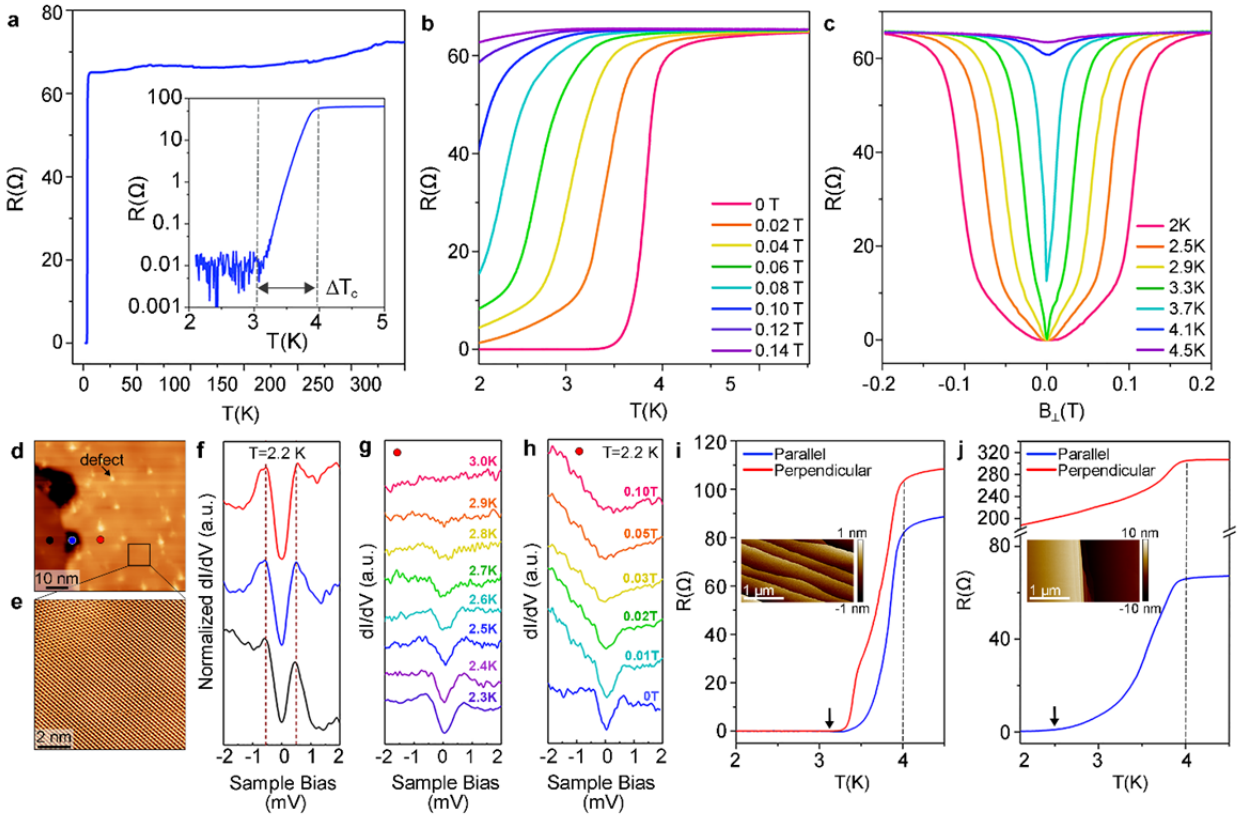

Figure 4: Superconductivity in 2D-Ga grown via confinement heteroepitaxy. (a) Zero-field R(T) curve for an optimized 2D-Ga (plasma-treated, small-step, parallel configuration) film from 300 to 2 K. Inset of (a): log-scale plot from 5 to 2 K of the same curve. (b) R(T) curves showing a degradation in T_c and increase in residual resistance at 2 K with increasing out-of-plane magnetic field. (c) Resistance vs out-of-plane magnetic field (R(B)) curves showing a similar degradation in the superconducting state with increasing temperature. The kink may be attributed to two superconducting phases, possibly from discrete 2L Ga nd 3L Ga regions, step-edge interactions, or distinct superconducting transitions within a 3L Ga region. Data shown in a-c is from the same sample and measurement configuration. (d-e) Large-area and atomic resolution scanning tunneling microscopy images of the EG surface topography, respectively. (f) Differential conductance (dI/dV) spectra (normalized to 3.0 K spectra) taken at 2.2 K for the 3 different regions shown in (d). (g,h) Temperature-dependent (zero-field) and perpendicular magnetic-field-dependent (2.2 K) dI/dV spectra, respectively, of the right-terrace in (f). (i,j) R(T) plots comparing perpendicular and parallel current directions performed on small-step and large-step samples (both plasma-treated), respectively. Black arrows indicate approximate T_c(zero) values, and dashed lines are meant to aid the eye (T = 4K

temperature of the pre-EG growth H_2 etch step,[32] or through the delivery of carbon to the SiC surface during EG growth to promote buffer layer nucleation and suppress mass transport across SiC that leads to step formation.[33,34]

When considering the electronic origin of the superconductivity in 2D Ga/SiC, each of the constituent materials appear to be poor superconductors: SiC is semiconducting, graphene is not heavily doped as in graphene intercalation compound superconductors, and 2D Ga exhibits nearly-free electron characters and thus would not lead to substantial T_c, since electron-lattice interactions are weak in nearly-free electron metals. We show using first-principles calculations that it is another Fermi surface manifold – small electron pockets around K – that mainly contributes to superconductivity. Using DFT, we calculate the electronic densities of states near the Fermi level for α, β, and bi-/tri-layer 2D-Ga (**Figure 5a,b**) and also the Eliashberg spectral function $\alpha^2F(\omega)$ for tri-layer $Ga_{Si}Ga_CGa_C$ epitaxial to SiC without the graphene cap (**Methods, Figure S19**). α-Ga contains Ga dimers whose incipient covalency suppresses the density of states near the Fermi level, while β-Ga recovers a more nearly free-electron-like behavior. **Figure 5c** compares $\alpha^2F(\omega)$ and the cumulative electron-phonon coupling strength $\lambda(\omega)$ to the projected phonon density of states for the three individual Ga layers and the interfacial Si atom. The dominant contributions to the overall λ=1.62 come from Ga vibrations below 120 cm^{-1}, with modest evidence near 180 cm^{-1} for distinct coupling channels specific to the (more covalent) lower layers of Ga and little sign of involvement from the interfacial Si. This is in contrast to previous reports attributing 2D superconductivity to interfacial bonding[35]. **Figure 5d** shows the momentum-resolved electron-phonon coupling[36] (λ_k) across the Ga/SiC Brillouin zone for electronic states within ±0.5 eV of the Fermi energy; (**Figure S19** provides a similar plot for a narrower energy range). Dominant contributions to λ_k come from electron pockets near the two symmetry-inequivalent K points. Further decomposition of $\lambda_{k=K}$ by phonon wavevectors show that the strongest contributions arise from intervalley scattering between the two K valleys (see discussion on **Figures S20 and S21**). Interestingly, this reciprocal-space structure to the coupling is similar to MoS_2, but here we have a p-block metal (with a large companion near-circular nearly-free-electron Fermi surface), with a small but crucial Fermi surface manifold with a doped semiconductor character. A set of six pockets are indeed clearly seen in the ARPES

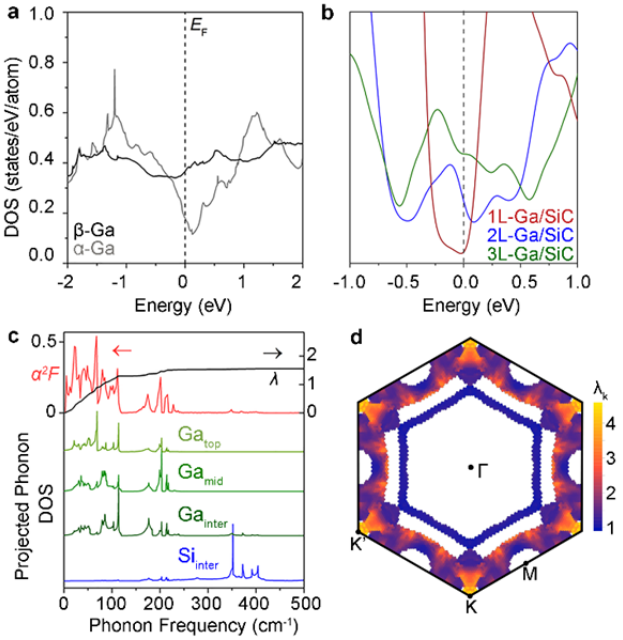

Figure 5: Theoretical calculations on graphene/2D-Ga heterostructures. (a) Electronic density of states (DOS) vs energy density functional theory (DFT) calculations for the two bulk phases of Ga including the stable α-Ga (low-Tc) and the metastable β-Ga (high-T_c) phases. (b) DOS vs energy calculations for 2L-Ga/SiC and 3L-Ga/SiC. (c) The Eliashberg spectral function $\alpha^2F(\omega)$ (red) compared with the projected phonon DOS of the three types of Ga atoms in trilayer Ga (shades of green) and the top Si atoms at the interface (blue). Importantly, the cumulative electron phonon coupling strength $\lambda(\omega)$ is superimposed in black at the top of (c). (d) Momentum-resolved electron-phonon coupling λ_k shows that the dominant contribution to coupling strength λ comes from the electron pockets near the K and K´ points in the Ga Brillouin zone. Graphene is not included in calculations.

measurement in **Figure 3c**, 30º rotated from the graphene Dirac points; they correspond to hole pockets near K in **Figure 3b** and 3e, and also similar in size to the pockets in the more accurate hybrid-functional-calculated bands of **Figure S11** (see discussions on **Figure S21** for details on the exact character of the pocket). The dominant contribution from these pockets is reassuring, since such strong coupling would not be expected from the more free-electron-like sheets of the Fermi surface. The Using the McMillian-Allen-Dynes formula[37,38] with λ=1.62 and μ^* from 0.1 to 0.15 yields a T_c of 3.5 to 4.1 K, in good agreement with experiment. Literature reports of the electron-phonon coupling strength in β-Ga suggest that it is also a reasonably strong-coupled superconductor[39], unlike more weakly coupled α-Ga[37].

The large λ=1.62 derived from the Ga states alone suggests that the EG layers are unlikely to be the driver of superconductivity in CHet-derived 2D-Ga. ARPES (**Figure 3**) provides further evidence towards this conclusion: the Fermi level is only 0.2–0.3 eV above the graphene Dirac point, corresponding to $n \approx 8\text{-}10 \times 10^{12}$ cm^{-2}, which is 10–100× lower than superconducting Li- or Ca-doped epitaxial graphene[40,41]. In those cases, superconductivity is attributed to a partially filled band near the Γ point at a much higher level of charge transfer into graphene than is observed in Ga-intercalated EG. Superconductivity in low-angle twisted bilayer graphene[42] likely exhibits a different origin from that in EG/Ga wherein the required interlayer twist is not present within the EG itself, although the environmental stability of 2D-Ga coupled with the controllable thickness of EG (1-3L post-intercalation) opens prospects to mechanically stack an additional (twisted) graphene monolayers onto EG/2D-Ga to create one of many hybrid superconducting systems possible based on the platform of highly stable CHet-derived 2D metals.

Conclusion

Confinement Heteroepitaxy (CHet) stabilizes 2D forms of 3D metals. The overlying graphene layers utilized in CHet not only help confine the 2D metals, but also serve as a hermetic seal to prevent oxidation of ultrathin non-noble metals, as revealed by the ability to perform extensive *ex situ* characterization of these materials. Whereas previously gold was arguably the only environmentally stable elemental metal, the realization of air-stable, single-crystal, elemental metals and superconductors at the interface of graphene and SiC opens the door to stabilizing diverse 2D allotropes of 3D metals and their alloys across the periodic table with potentially novel properties, all of which are candidates for incorporation into advanced multi-component heterostructures for next-generation quantum[3], photonic[43], and electronic applications.

Acknowledgements

Funding for this work was provided by the Northrop Grumman Mission Systems' University Research Program, Semiconductor Research Corporation Intel/Global Research Collaboration Fellowship Program, task 2741.001, NSF CAREER Awards 1453924 and 1847811, the Chinese Scholarship Council, an Alfred P. Sloan Research Fellowship, NSF DMR-1708972 and 1808900, and the 2D Crystal Consortium National Science Foundation (NSF) Materials Innovation Platform under cooperative agreement DMR-1539916. A portion of this research was conducted at the Center for Nanophase Materials Sciences, which is a DOE Office of Science User Facility, and at the Pennsylvania State University Materials Research Institute's Material

Characterization Laboratory. This research used resources of the Advanced Light Source, which is a DOE Office of Science User Facility under contract no. DE-AC02-05CH11231.

Contributions

N.B, B.B., Y.W., V.C., and J.A.R. wrote the paper with input from co-authors. N.B. performed the intercalation growths and XPS characterization and assisted in Raman spectroscopy and SEM characterization. B.B performed Raman spectroscopy and SEM characterization and assisted in sample preparation and electrical characterization. Y.W. performed DFT modeling of EG/Ga/SiC heterostructures in consultation with V.C. with input from J.Z., B.B., N.B., and J.A.R. J.J. performed electrical measurements under the direction of C.Z.C. with input from B.B and J.Z. R.K., A.B., and C.J. performed ARPES measurements under direction of E.R. N.N. performed graphene defect modeling under the direction of A.vD. K.W. performed cross-sectional STEM imaging. M.K. and W.K. prepared LEED tool for EG/metal/SiC samples and M.K. performed LEED measurements. A.D.L.F.D. performed intercalation growths and assisted with material characterization. C.D. and S.S. performed the graphene synthesis under the direction of J.A.R. J.S. assisted in XPS data analysis. M.F., Q.Z., G.Z., and A.P.L. performed scanning probe characterization. Y.W.C assisted with electrical measurements under the direction of J.Z. The authors would also like to acknowledge Haiying Wang for help with STEM sample cross-section preparation via FIB, Vince Bojan, Nabil Bassim, and Heshem Elsherif for help with Auger electron spectroscopy, and Max Wetherington for Raman spectroscopy support.

Methods

Epitaxial Graphene Synthesis and Plasma Treatment

Epitaxial graphene is synthesized via silicon sublimation from the (0001) plane of semi-insulating 6H-SiC (II-VI Inc.) at 1800°C, 700 Torr Argon, for 15 min (Ref.13, SI). Graphene layers were plasma treated using a Tepla M4L plasma etch tool, using 150 sccm O_2 and 50 sccm He under a pressure of 500 mTorr and power of 50 W for 60 seconds.

2D-Metal Intercalation

Metal intercalation was performed using an STF-1200 horizontal tube furnace fitted with a 1" outer diameter quartz tube. A custom-made alumina crucible from Robocasting Enterprises LLC. was used to hold 1x1cm EG/SiC substrates, which were placed with graphene layers on the Si face of SiC facing downward, toward the inside of the crucible. 30-60 mg of metallic Ga (Sigma Aldrich, 99.999%), In powder (Alfa Aesar, -325 mesh, 99.99%), or Sn granules (Alfa Aesar, 99.5%) were placed in the crucible, directly beneath the EG/SiC substrate. The crucible with EG/SiC and the respective metal precursor was then loaded into the tube furnace and evacuated to ~5 mTorr. The tube is then pressurized to 300-700 Torr with Ar. At this time, the furnace was heated to 700-800°C under a ramp rate of 20°/minute and Ar flow of 50 sccm. The furnace was held at the growth temperature for 30 minutes, then cooled to room temperature.

X-ray photoelectron spectroscopy

X-ray photoelectron spectroscopy measurements were carried out with a Physical Electronics Versa Probe II equipped with a monochromatic Al K_α X-ray source (hν=1486.7 eV) and a concentric hemispherical analyzer. High resolution spectra were obtained over an analysis area of 200 μm at a pass energy of 29.35 eV for C 1s, Si 2p, Ga 3d, and Ga 2p regions. O 1s regions were collected with a pass energy of 46.95 eV. The acquired spectra were fitted Lorentzian line shapes, and the asymmetric graphene peak fit was derived from exfoliated highly oriented pyrolytic graphite and H-intercalated epitaxial graphene reference samples. Spectra were charge referenced to this graphene peak in C 1s corresponding to 284.5 eV. A U 2 Tougaard background was used to fit XPS spectra.

Raman spectroscopy

Raman Spectroscopy is performed with a Horiba LabRam Raman system using a wavelength of 488nm and a power of 4.6 mW. Spectra are acquired with an integration time of 30s, using a 600 grooves/mm grating.

Cross-sectional transmission electron microscopy

Cross-sectional samples for STEM imaging were prepared by *in situ* lift-out via milling in a FEI Helios NanoLab DualBeam 660 focused ion beam (FIB). Prior to FIB, ~40/5/10 nm of SiO_2/Ti/Au was deposited via electron-beam evaporation in a Kurt J. Lesker Lab18 evaporator, to improve contrast during STEM imaging at low magnifications. Cross-sections were prepared using a Ga^+ ion beam at 30 kV then stepped down to 1 kV to avoid ion beam damage to the sample surface.

High resolution scanning transmission electron microscopy (STEM) of sample cross sections was performed in a FEI dual aberration corrected Titan3 G2 60-300 S/TEM at 200kV using a high angle annular dark field (HAADF) detector. The HAADF detector (Fischione) has a collection angle of 51-300 mrad for Z-contrast imaging. A beam current of 70pA, beam convergence of 30 mrad (C2 aperture of 70 μm), and camera length of 115 mm are used for STEM image acquisition. The STEM EDS maps are collected by using the superX EDS system, which has 4 EDS detectors surrounding the sample.

Low-energy electron diffraction

Low-energy electron diffraction measurements of EG/Ga/SiC, EG/In/SiC, and EG/Sn/SiC samples were performed using LEED Spectrometer BDL800IR-MCP manufactured by OCI Vacuum Microengineering. Samples were first degassed at 200°C for 30 minutes under UHV to desorb surface moisture and contaminants. LEED patterns were then acquired at room temperature using constant primary beam currents of 10 nA and beam energies of 50 eV – 250 eV, in 1 eV steps.

Angle-resolved photoemission spectroscopy

Angle-resolved photoemission spectroscopy measurements were performed at the Microscopic and electronic structure observatory (MAESTRO) beamline at the Advanced Light Source at Lawrence Berkeley National Lab. The sample was annealed at 550 K for 30 minutes in the end-station before measurements to remove adsorbates from the transfer of the sample through air. Measurements of EG/Ga/SiC and Gr/In/SiC structures were performed using a photon energy of 140 eV and 110 eV, respectively. Photoemission spectra were collected by moving the sample around one angle while using the angle resolved mode of a Scienta R4000 electron analyzer for the collection of the other angular axis.

Transport measurements and T_c, B_c, and T_{BKT} extraction:

Transport measurements were carried out in a Quantum Design physical property measurement system (PPMS) system. Contacts were made to the graphene/Ga heterostructure by lightly scratching the film surface with a diamond scribe or tweezers, and then lightly pressing or soldiering indium dots onto the scratched region. This was done in a casual attempt to make side-contact to the 2D-Ga. Indium dots were arrayed in a standard co-linear four-point-probe configuration with contact pitch on the order of hundreds of microns. All resistance measurements were made with an excitation current of 1 μA. T_c(onset) is defined as the intersection of linear extrapolations of the transition and normal regions. The linear fit for the transition region is the region of maximum slope, which is consistent for the entire transition width as seen in the log plot inset in **Figure 4a**. $T_c(0.5R_N)$ is defined as the temperature at which the sample reaches half of its normal resistance. T_c(zero) is defined as the temperature at which resistance effectively reaches a zero-resistance state i.e. the noise floor of the PPMS system ~ 0.01 Ω. The transition width ΔT_c is defined as the change in temperature between the T_c(onset) and T_c(zero). Various T_c values are provided in order to help comparison with other works in literature which may use different values. Critical field

$B_{c2}(0.9R_N)$ is defined as the magnetic field at which the sample reaches 90% of its normal resistance. Coherence length is estimated from $B_{c2}(T) = \frac{\Phi}{2\pi\xi_0^2}$.

Scanning tunneling spectroscopy/microscopy (STS/STM):
Ga-intercalated graphene/SiC was studied using ultra-high vacuum low-temperature scanning tunneling microscope with *in situ* out of plane magnetic field at the Center for Nanophase Materials Sciences at Oak Ridge National Laboratory. The sample was preheated to 200°C to remove surface adsorbates at UHV with a base pressure of 2×10^{-10} Torr before transferring *in situ* to STM stage. STM/S was conducted using mechanically cut Pt-Ir tip. All Pt-Ir tips were conditioned and checked using clean Au (111) surface before each measurement. Topographic images were acquired in constant current mode with the bias voltage applied to the samples. All the spectroscopies were obtained using the lock-in technique with bias modulation at 973 Hz. The STM image in **Figure 4d** was taken at V_b = 10 mV and I_t = 400 pA. The STM image in **Figure 4e** was taken at V_b = -100 mV, I_t = 100 pA. The dI/dV spectra in **Figures 4f-h** were measured at V_b = 5 mV, I_t = 400 pA, and ΔV = 0.1 mV.

Theory

i. Graphene defect generation/passivation and Ga adsorption: All density functional theory calculations investigating the role of plasma treatment on EG defects and Ga intercalation were performed in Quantum Espresso (SI ref. 14), using projected augmented wave pseudopotentials (SI ref. 15, 16) and the Perdew-Burke-Ernzerhof parametrization of the generalized gradient approximation exchange-correlation functional (GGA-PBE, SI ref. 17, 18). A 5×5×1 Γ-centered k-point mesh was applied for Brillouin zone integration. Planewave expansions were truncated at an energy cut-off of 408 eV for wavefunctions and at 4080 eV for charge densities. The Marzari-Vanderbilt cold smearing scheme (SI ref. 19) was applied with a broadening of 0.1 eV. Structural relaxations used the Broyden–Fletcher–Goldfarb–Shanno algorithm with a force threshold of 0.025 eV/Å. A vacuum layer of 20 Å was inserted in the direction normal to the graphene sheets to minimize the spurious interactions across the periodic boundary. The models in the figures were visualized using OVITO (SI ref. 20) and VESTA (SI ref. 21) software.

ii. 2D Ga phase stability and electronic structure calculations: All density functional theory calculations on phase stabilities and electronic structure were performed using the GGA-PBE exchange-correlation functional (SI ref. 17) and the projector augmented wave (PAW) pseudopotentials (SI ref. 15,16). Plane-wave expansions were truncated at an energy cutoff of 500 eV. All structural relaxations were performed using dipole corrections to the total energy (SI ref. 22) and to the electrostatic potential (SI ref. 23) in the out-of-plane direction, until the remaining forces are within 0.01 eV/Å. Brillouin zone samplings are performed on grids with k-point densities equivalent to that of a 20×20×1 grid for a 1×1 Ga/SiC unit cell. All Ga/SiC calculations were performed using 7 repeating units of SiC along the *z* direction as substrate, capped by Ga from above and by hydrogen from below. Graphene/Ga/SiC calculations were performed using 5 repeating units along the *z* direction for the a 2×2 graphene + √3×√3 R30º Ga/SiC supercell, and 3 repeating units for the a 5×5 graphene + 4×4 R0º Ga/SiC supercell to alleviate the computational demand of accommodating more atoms in the large supercells. Band unfolding were performed using the GPAW package (SI ref. 24); all other calculations were performed by the Vienna Ab Initio Package (VASP) (SI ref. 25). Fermi surfaces of Ga/SiC are calculated on a 40×40×1 grid and interpolated onto a 200×200×1 grid for plotting. Band structures at the hybrid functional level were calculated using the range-separated form of Heyd, Scuseria, and Ernzerhof (SI ref. 26) (HSE06, i.e. with a range-separation parameter of 0.2 $Å^{-1}$) and using structures relaxed at the PBE level. Self-consistent HSE06 calculations were performed on a 12×12×1 k-point grid. In **Figure 5b**, bilayer and trilayer Ga on SiC exhibits a DOS at E_F similar to β-Ga (**Figure 5a**), where for bilayer Ga we artificially shift E_F by 0.5 eV to account for

the additional (undetermined) electron doping so the band alignment agrees with ARPES measurements. As for the DOS calculations carried out on hexagonal 2L and 3L-Ga/SiC, the $Ga_{Si}Ga_{C}$ and $Ga_{Si}Ga_{C}Ga_{C}$ stacking sequences were used, respectively. The $Ga_{Si}Ga_{C}Ga_{C}$stacking sequence occupies one of the lower energy configurations out of all the possible stacking sequences for 3L-Ga and most closely matches the band structure as directly measured in ARPES (**Figures S10-11, Table S1**. Thus, $Ga_{Si}Ga_{C}$ and $Ga_{Si}Ga_{C}Ga_{C}$ stackings were used to calculate the DOS and the $Ga_{Si}Ga_{C}Ga_{C}$ stacking was used to calculate T_c (**Figure S18a**).

iii. Electron-phonon interactions: All calculations related to electron-phonon interactions are performed in a cell with only two SiC units, due to the heavy computational demand of these routines; SiC slabs are passivated from below by H atoms with the same mass as Si. The starting-point electronic charge density is calculated on a 12×12×1 Γ-centered k-point grid. Electronic wavefunctions are then computed for a 6×6×1 grid. The phonon dispersion is calculated using density functional perturbation theory based on the same 6×6×1 grid. All computations above are performed by the Quantum ESPRESSO package using the local density approximation exchange-correlation functional, Hartwigsen-Goedeker-Hutter norm-conserving pseudopotentials, and a plane wave expansion cutoff of 1090 eV. To achieve a dense sampling of electron-phonon coupling matrix elements across the Fermi surface, we construct electronic and phonon Wannier functions based on wavefunctions and phonon modes sampled on the coarse 6×6×1 grid and generate interpolations onto a 96×96×1 grid, as implemented by the EPW code. Wannier functions are initialized by projecting the following orbitals onto Bloch wavefunctions: two *s* and one p_z for each Ga, one sp^3 orbital for each Si, and one sp^3 for each C. An outer disentanglement window (i.e. one that captures all targeted bands with the chosen orbital characters) coincides with the entire energy range (**Figure S18b**). An inner window (where all Bloch states are included within the projection manifold) spans the energy range from the lower bound of **Figure 18b** up to 1 eV above the Fermi level. See **SI** for more details on equations and references used.

Data availability

The data that support the findings of this study are available from the authors on reasonable request, see author contributions for specific data sets.

References

1. Rhodes, D., Chae, S. H., Ribeiro-Palau, R. & Hone, J. Disorder in van der Waals heterostructures of 2D materials. *Nat. Mater.* **18,** 541–549 (2019).
2. Al Balushi, Z. Y. *et al.* Two-dimensional gallium nitride realized via graphene encapsulation. *Nat. Mater.* **15,** 1166–1171 (2016).
3. Fu, L. & Kane, C. L. Superconducting Proximity Effect and Majorana Fermions at the Surface of a Topological Insulator. *Phys. Rev. Lett.* **100,** 096407 (2008).
4. Maniyara, R. A. *et al.* Tunable plasmons in ultrathin metal films. *Nat. Photonics* **13,** 328–333 (2019).
5. Shah, D., Reddy, H., Kinsey, N., Shalaev, V. M. & Boltasseva, A. Optical Properties of Plasmonic Ultrathin TiN Films. *Adv. Opt. Mater.* **5,** 1700065 (2017).
6. Riedl, C., Coletti, C. & Starke, U. Structural and electronic properties of epitaxial Graphene on SiC(0001): A review of growth, characterization, transfer doping and hydrogen intercalation. *J. Phys. D. Appl. Phys.* **43,** 374009 (2010).
7. Emtsev, K. V, Zakharov, A. A., Coletti, C., Forti, S. & Starke, U. Ambipolar doping in quasifree epitaxial graphene on SiC (0001) controlled by Ge intercalation. *Phys. Rev. B* **84,** 125423 (2011).
8. Gierz, I. *et al.* Electronic decoupling of an epitaxial graphene monolayer by gold

intercalation. *Phys. Rev. B* **81,** 235408 (2010).
9. Virojanadara, C., Watcharinyanon, S., Zakharov, A. A. & Johansson, L. I. Epitaxial graphene on 6H-SiC and Li intercalation. *Phys. Rev* **82,** 205402 (2010).
10. Subramanian, S. *et al.* Properties of synthetic epitaxial graphene/molybdenum disulfide lateral heterostructures. *Carbon N. Y.* **125,** 551–556 (2017).
11. Moulder, J. F. & Chastain, J. *Handbook of x-ray photoelectron spectroscopy : a reference book of standard spectra for identification and interpretation of XPS data*. (Physical Electronics Division, Perkin-Elmer Corp, 1992).
12. Beamson, G. (Graham) & Briggs, D. (David). *High resolution XPS of organic polymers : the Scienta ESCA300 database*. (Wiley, 1992).
13. Eckmann, A. *et al.* Probing the Nature of Defects in Graphene by Raman Spectroscopy. *Nano Lett.* **12,** 3925–3930 (2012).
14. Vishwakarma, R. *et al.* Transfer free graphene growth on SiO2 substrate at 250 °C. *Sci. Rep.* **7,** 43756 (2017).
15. Araby, M. I. *et al.* Graphene formation at 150°C using indium as catalyst. *RSC Adv.* **7,** 47353–47356 (2017).
16. Fujita, J. *et al.* Near room temperature chemical vapor deposition of graphene with diluted methane and molten gallium catalyst. *Sci. Rep.* **7,** 12371 (2017).
17. Yi, C. *et al.* Evidence of Plasmonic Coupling in Gallium Nanoparticles / Graphene / SiC. *Small* **8,** 2721–2730 (2012).
18. Losurdo, M. *et al.* Demonstrating the Capability of the High-Performance Plasmonic Gallium-Graphene Couple. *ACS Nano* **8,** 3031–3041 (2014).
19. Khorasaninejad, M. *et al.* Highly Enhanced Raman Scattering of Graphene using Plasmonic Nano-Structure. *Sci. Rep.* **3,** 1–7 (2013).
20. Voloshina, E., Rosciszewski, K. & Paulus, B. First-principles study of the connection between structure and electronic properties of gallium. *Phys. Rev. B* **79,** 045113 (2009).
21. Ashcroft, N. W. & Mermin, N. D. *Solid state physics (p. 38)*. (Holt, Rinehart and Winston, 1976).
22. Yoshizawa, S., Kim, H., Hasegawa, Y. & Uchihashi, T. Disorder-induced suppression of superconductivity in the Si(111)-(7 × 3) -In surface: Scanning tunneling microscopy study. *Phys. Rev. B - Condens. Matter Mater. Phys.* **92,** 041410 (2015).
23. Yang, L., Deslippe, J., Park, C.-H., Cohen, M. L. & Louie, S. G. Excitonic Effects on the Optical Response of Graphene and Bilayer Graphene. *Phys. Rev. Lett.* **103,** 186802 (2009).
24. Zhang, Y., Tan, Y.-W., Stormer, H. L. & Kim, P. Experimental observation of the quantum Hall effect and Berry's phase in graphene. *Nature* **438,** 201–204 (2005).
25. Popescu, V. & Zunger, A. Extracting E versus $\vec{k}$ effective band structure from supercell calculations on alloys and impurities. *Phys. Rev. B* **85,** 085201 (2012).
26. Gregory, W. D., Sheahen, T. P. & Cochran, J. F. Superconducting Transition and Critical Field of Pure Gallium Single Crystals. *Phys. Rev.* **150,** 315–321 (1966).
27. Chen, T. T., Chen, J. T., Leslie, J. D. & Smith, H. J. T. Phonon Spectrum of Superconducting Amorphous Bismuth and Gallium by Electron Tunneling. *Phys. Rev. Lett.* **22,** 526–530 (1969).
28. Wühl, H., Jackson, J. E. & Briscoe, C. V. Superconducting Tunneling in the Low-Temperature Phases of Gallium. *Phys. Rev. Lett.* **20,** 1496–1499 (1968).
29. Parr, H. & Feder, J. Superconductivity in β-Phase Gallium. *Phys. Rev. B* **7,** 166–181

(1973).
30. Werthamer, N. R. Theory of the Superconducting Transition Temperature and Energy Gap Function of Superposed Metal Films. *Phys. Rev.* **132,** 2440–2445 (1963).
31. Reyren, N. *et al.* Superconducting interfaces between insulating oxides. *Science* **317,** 1196–9 (2007).
32. M. H. Oliveira, Jr., T. Schumann, M. Ramsteiner, J. M. J. Lopes, and H. R. Influence of the silicon carbide surface morphology on the epitaxial graphene formation. *Appl. Phys. Lett.* **99,** 111901 (2011).
33. Kruskopf, M. *et al.* A morphology study on the epitaxial growth of graphene and its buffer layer. *Thin Solid Films* (2018). doi:10.1016/j.tsf.2018.05.025
34. Mattias Kruskopf1 *et al.* Comeback of epitaxial graphene for electronics: large-area growth of bilayer-free graphene on SiC. *2D Mater.* **3,** 041002 (2016).
35. Zhang, T. *et al.* Superconductivity in one-atomic-layer metal films grown on Si(111). *Nat. Phys.* **6,** 104–108 (2010).
36. Margine, E. R. & Giustino, F. Anisotropic Migdal-Eliashberg theory using Wannier functions. *Phys. Rev. B* **87,** 024505 (2013).
37. McMillan, W. L. Transition Temperature of Strong-Coupled Superconductors. *Phys. Rev.* **167,** 331–344 (1968).
38. Allen, P. B. & Dynes, R. C. Transition temperature of strong-coupled superconductors reanalyzed. *Phys. Rev. B* **12,** 905–922 (1975).
39. Garno, J. P. Simple high vacuum evaporation system with low□temperature substrate. *Rev. Sci. Instrum.* **49,** 1218–1220 (1978).
40. Ludbrook, B. M. *et al.* Evidence for superconductivity in Li-decorated monolayer graphene. *Proc. Natl. Acad. Sci. U. S. A.* **112,** 11795–9 (2015).
41. Ichinokura, S., Sugawara, K., Takayama, A., Takahashi, T. & Hasegawa, S. Superconducting Calcium-Intercalated Bilayer Graphene. *ACS Nano* **10,** 2761–2765 (2016).
42. Cao, Y. *et al.* Unconventional superconductivity in magic-angle graphene superlattices. *Nature* **556,** 43–50 (2018).
43. Boltasseva, A. & Shalaev, V. M. Transdimensional Photonics. *ACS Photonics* **6,** 1–3 (2019).